photonics

Article

A Design of All-Optical Integrated Linearized Modulator Based on Asymmetric Mach-Zehnder Modulator

Yiru Zhao [1,2], Jinye Li [1], Zichuan Xiang [1,2] and Jianguo Liu [1,2,*]

[1] State Key Laboratory on Integrated Optoelectronics, Institute of Semiconductors, Chinese Academy of Sciences, Beijing 100083, China
[2] College of Materials Science and Opto-Electronic Technology, University of Chinese Academy of Sciences, Beijing 100049, China
* Correspondence: jgliu@semi.ac.cn

Abstract: We proposed an all-optical linearized modulator model suitable for an integration platform. The linearized modulator is formed by an asymmetric Mach–Zehnder modulator and a carrier-separated waveguide. We focus on the suppression of both intermodulation distortion (IMD3) and second-order harmonic distortions (SHD). As a result, the third-order nonlinear terms of IMD3 and second-order nonlinear terms of SHD are entirely suppressed, leading to a spurious free dynamic range of IMD3 ($SFDR_{IMD3}$) improvement of ~14 dB and $SFDR_{SHD}$ improvement of ~3 dB compared with a standard MZM model. The influence of large RF input signals, losses, and fabrication deviations are also discussed to prove the feasibility of the model.

Keywords: linearity; integrated modulator; asymmetric Mach-Zehnder interferometer

check for updates

Citation: Zhao, Y.; Li, J.; Xiang, Z.; Liu, J. A Design of All-Optical Integrated Linearized Modulator Based on Asymmetric Mach-Zehnder Modulator. *Photonics* **2023**, *10*, 229. https://doi.org/10.3390/photonics10030229

Received: 28 January 2023
Revised: 14 February 2023
Accepted: 19 February 2023
Published: 21 February 2023

1. Introduction

Microwave photonics (MWP) has received extensive attention in recent years with the advantages of both the microwave and the photonics fields [1–3]. Modern MWP links have become increasingly crucial as higher-order QAM coherent systems become more analog-like and require a higher linear transmitter [4]. Prevalent microwave photonic links employ a direct detection (DD) scheme in which Mach–Zehnder modulators (MZMs) are widely used. However, the sinusoidal transmission characteristics of the MZM are the main limiting factor in the linearity of the MWP links, which restricts the spurious free dynamic range (SFDR). Therefore, it is highly desirable to develop a high-linearity modulator to propel the development of MWP systems.

Many MZM linearization methods have been suggested and implemented, which can be broadly categorized as electrical, mixed, and all-optical. Electrical linearization can achieve ultra-high SFDR at low frequency, but the bandwidth is limited by the speed of electronic processing [5–8]. The third-order nonlinearity is eliminated in silicon modulators built in a regular MZM configuration by optimizing doping [9]. However, this is not applicable to material platforms with a linear electro-optic effect. The mixed linearized modulator typically uses a dual-parallel Mach–Zehnder modulator (DPMZM) [10–13] to produce complimentary third-order intermodulation distortion (IMD3), as it cancels the IMD3 at the detector. However, a mixed linearized modulator requires precise control of the optical power splitter ratio, broadband microwave attenuator, and phase shifter. All-optical linearization includes discrete links and integrated modulators. The discrete all-optical linearization is ultra-wideband and wavelength-independent, but it requires an attenuator to eliminate the IMD3, which causes unwanted signal attenuation [14]. The integrated linearized modulators mainly utilize a micro-ring [15–21] or Bragg grating [22] to improve the interference characteristic of the Mach–Zehnder interferometers (MZIs), which have been successfully implemented on the Silicon Photonics platform. These integrated modulators are attractive for their simplicity and robustness, but the resonators limit the bandwidth.

In this paper, we propose an all-optical linearization design for the integrated modulator. The linearized modulator is formed by an asymmetric Mach–Zehnder modulator and a carrier-separated waveguide, called carrier separated asymmetric Mach–Zehnder modulator (CS-AMZM). A mathematical model is built to investigate the linearity of the CS-AMZM structure. The second-order harmonic distortions (SHDs) and IMD3 can be suppressed simultaneously at a specific operating point to achieve a spurious-free status within the full operating broadband. At the same time, CS-AMZM does not contain resonators, so its operating bandwidth can be close to MZM. Through calculation and simulation, the SFDR_{SHD} of CS-AMZM is close to MZM, and the $\text{SFDR}_{\text{IMD3}}$ is ~14 dB higher than the standard MZM. In the case of large input power, the harmonics can be further suppressed by feedback control. In addition, after considering the leading design and process errors in fabrication, it is revealed that the performance is almost consistent with the ideal case except for loss.

2. Linearized CS-AMZM Model

The nonlinearity effect of a modulator is usually represented by the two-tone test. The modulator is driven by two signals whose frequencies are closely spaced. Because of the nonlinear electro-optic response of the modulator, the output optical signal contains new frequency components called intermodulation distortions (IMDs) and harmonic distortions (HDs). The nonlinearity calculation usually only considers the IMD3 but ignores the SHD, which limits the system within the range of the sub-octave bandwidth. To improve the system's performance, the SHD is also a factor that must be considered. Therefore, the SHD and IMD3 need to be suppressed simultaneously, and the loss of (first-order harmonics) FH components should also be minimized.

We first consider the ideal model of an AMZM, as shown in Figure 1. The difference between AMZM and MZM is that the power ratio of the input beam splitter is unequal. Directional coupler splitter (DCS), 1 × 2 MZI, asymmetric Y branch, and arbitrary ratio MMI [23–25] are all suitable choices for asymmetric beam splitters. In this paper, DCS is chosen for calculation and design. The power ratio of the splitter is t^2: k^2, and of course, $t^2 + k^2 = 1$. The input optical field of the AMZM is $E_{in} = E_0\exp(j\omega t)$, and the driving signals of the two arms (WG-A1 and WG-A2) consist of a two-tone signal and a direct current bias, written as:

$$\begin{aligned} V_1 &= V_{DC} + v_0(\cos\omega_1 t + \cos\omega_2 t) \\ V_2 &= -v_0(\cos\omega_1 t + \cos\omega_2 t), \end{aligned} \tag{1}$$

where v_0 is the amplitude of the RF signal and V_{DC} is the direct current bias voltage. ω_1 and ω_2 are the angular frequencies of the two-tone signal. Here, to simplify the calculation, we let DC voltage only exist in the upper arm, which does not affect the correctness of the calculation. The phase difference between WG-A1 and WG-A2 caused by the DCS can be ignored owing to V_{DC}, which can achieve any desired operating points. Therefore, V_{DC} will directly represent the phase difference between WG-A1 and WG-A2. The modulated optical field of the two arms can be written as:

$$\begin{aligned} E_1 &= E_0 t\exp(j(\omega t + x_{DC} + x_0(\cos\omega_1 t + \cos\omega_2 t))) \\ E_2 &= E_0 k\exp(j(\omega t - x_0(\cos\omega_1 t + \cos\omega_2 t))), \end{aligned} \tag{2}$$

where $x_0 = \pi v_0/V_\pi$ and $x_{DC} = \pi V_{DC}/V_\pi$ are the modulator index of the RF signal and DC bias, respectively. V_π is the half-wave voltage of the AMZM. We normalize E_0 to 1 and set the operating point of AMZM to $\exp(jx_{DC}) = j$. In addition, only linear electro-optic materials are considered here, such as lithium niobate (LN). The modulation of voltage to phase is linear and ignores asymmetries of WG-A1 and WG-A2. The modulation sidebands are calculated using Bessel expansion. Following this, the coefficients of the sidebands related to the FH, SHD, and IMD3 in the E_{out} can be written as:

$$\begin{aligned}
&[0]: \ W_0 = \tfrac{1}{2}(jt+k)J_0^2 \\
&[\pm\omega_1, \pm\omega_2]: \ W_1 = -\tfrac{1}{2}(t+jk)J_0J_1 \\
&[\pm 2\omega_1, \pm 2\omega_2]: \ W_2 = -\tfrac{1}{2}(jt+k)J_0J_2 \\
&[\pm(\omega_1-\omega_2)]: \ W_{11} = -\tfrac{1}{2}(jt+k)J_1^2 \\
&[\pm(2\omega_1-\omega_2), \pm(2\omega_2-\omega_1)]: \ W_{21} = \tfrac{1}{2}(t+jk)J_1J_2,
\end{aligned} \tag{3}$$

where W_i is the power of the corresponding sideband. J_n is a simplified form of $J_n(x_0)$, which is the n-order Bessel function of the first kind, and $[\pm\omega_i]$ represents $\exp(j\omega t \pm j\omega_i t)$. For square-law detectors, the photocurrent of the FH, SHD, and IMD3 components can be calculated by the modulation sidebands (see Appendix A):

$$\begin{aligned}
I_{FH} \quad &\sim \left|W_0W_1^* + W_1W_0^*\right| \\
&= tkJ_0^3J_1 \approx \tfrac{1}{2}tkx_0 \\
I_{SHD} \quad &\sim \left|2(W_0W_2^* + W_2W_0^*) + W_1W_1^* + W_1W_1^*\right| \\
&= (t^2+k^2)\left(\tfrac{1}{2}J_0^2J_1^2 - J_0^3J_2\right) \approx 0 \\
I_{IMD3} \quad &\sim \left|W_0W_{21}^* + W_{21}W_0^* + W_1W_{11}^* + W_{11}W_1^* + W_1W_2^* + W_2W_1^*\right| \\
&= tk\left(J_0^2J_1J_2 + \tfrac{1}{2}J_0J_1^3\right) \approx \tfrac{1}{8}tkx_0^3,
\end{aligned} \tag{4}$$

where the Bessel function is approximated by a power series expansion under the case of the small signal; it can be seen in Equation (4) that for AMZM, although the SHD is almost nonexistent, neither FH nor IMD3 have zero points. If a cancellation component can be introduced, the FH and IMD3 components can obtain different zero points. Therefore, a carrier-separated AMZM (CS-AMZM) is proposed, as seen in Figure 2.

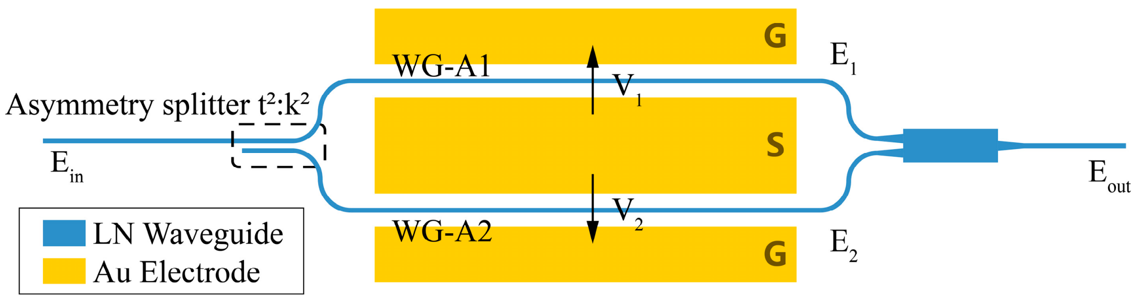

Figure 1. A schematic diagram of the single AMZM.

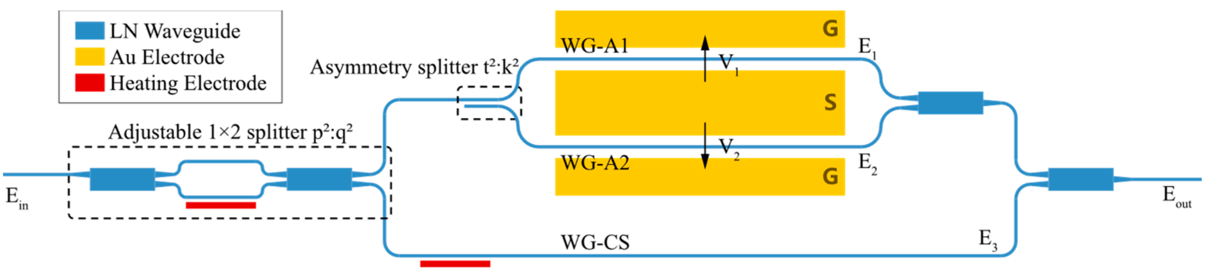

Figure 2. A schematic diagram of the single CS-AMZM.

For IMD3 components to obtain zero points, we add an adjustable 1×2 splitter to separate a portion of the carrier, whose power ratio is p^2: q^2, $p^2 + q^2 = 1$. The arm for the separated carrier, called WG-CS, has a heating electrode to control the phase shift, which is defined as $\Delta\phi$. It should be noted that the adjustable 1×2 splitter will introduce a phase difference of π on the two arms. $\Delta\phi$ includes this phase difference, and represents the total phase difference between the two output ports. The optical field of WG-A1, WG-A2, and the WG-CS can be written as:

$$\begin{aligned} E_1 &= pt\exp(jx_{DC})\exp(j\omega t + jx_0(\cos\omega_1 t + \cos\omega_2 t)) \\ E_2 &= pk\exp(j\omega t - jx_0(\cos\omega_1 t + \cos\omega_2 t)) \\ E_3 &= q\exp(j\Delta\phi), \end{aligned} \tag{5}$$

The photocurrent of the FH, SHD, and IMD3 components can be written as

$$\begin{aligned} I_{FH} &\sim \tfrac{1}{2}p\left|2pkt + \sqrt{2}q(t\cos\Delta\phi + k\sin\Delta\phi)\right|x_0 \\ I_{SHD} &\sim \tfrac{\sqrt{2}}{4}pq|k\cos\Delta\phi + t\sin\Delta\phi|x_0^2 \\ I_{IMD3} &\sim \tfrac{1}{64}p\left|8ptk + \sqrt{2}q(k\cos\Delta\phi + t\sin\Delta\phi)\right|x_0^3, \end{aligned} \tag{6}$$

It can be seen in Equation (6) that, after separating the carrier, the SHD and IMD3 components can exist with different zero points with a suitable $\Delta\phi$.

Figure 3 shows the I_{FH}, I_{SHD}, and I_{IMD3} in Equation (6) changed with the power ratio of the two splitters when $\Delta\phi = 7/8\pi$. The zero points of SHD and IMD3 components are marked with a dotted black line and solid black line, respectively. x_0 is set to 0.001, which is small enough to satisfy small-signal conditions. It should be noted that as for t, p = 0, or 1, CS-AMZM equivalents to a phase modulator, a waveguide, or a single AMZM, so the ranges of t^2 and p^2 are limited from 0.001 to 0.999. It can be seen that the variation in SHD is independent of t^2. SHD and IMD3 have a unique common zero point. Since Figure 3 will change with $\Delta\phi$, in order to find the maximum value of FH, we performed the calculation for different $\Delta\phi$s.

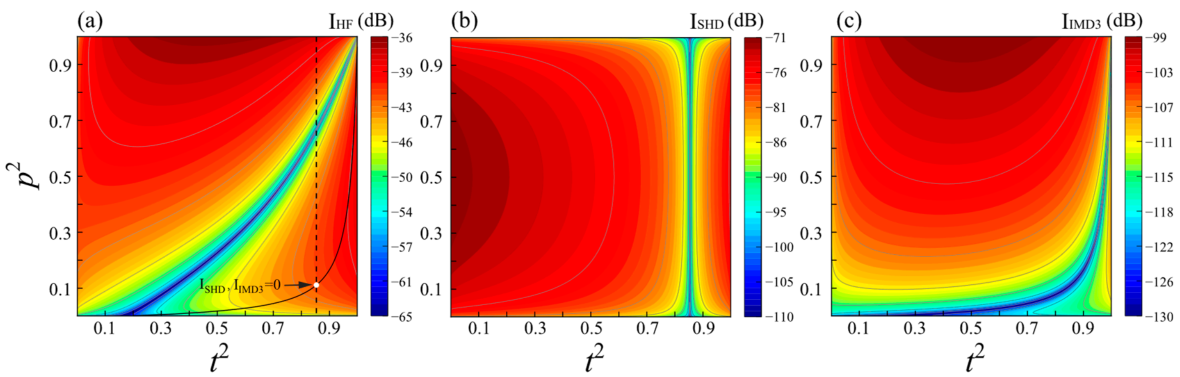

Figure 3. Contour map of the (**a**) I_{FH}, (**b**) I_{SHD}, and (**c**) I_{IMD3} as a function of t^2 and p^2 when $\Delta\phi = 7/8\pi$. The dotted and solid black lines in (**a**) mark the zeros points of the I_{SHD} and I_{IMD3}, respectively. The white point marks the common zero points of I_{SHD} and I_{IMD3}.

The common zero point of SHD and IMD3 changes as $\Delta\phi$ changes, as shown in Figure 4a. When $\Delta\phi$ is in a specific range, SHD and IMD3 have a common zero point. It is independent of p to suppress SHD for a certain $\Delta\phi$. Therefore, t can be fixed with a specific splitter structure. The FH power reaches its maximum when $\Delta\phi = 7.6/8\pi$, as shown in Figure 4b. In actual fabrication, it is difficult to make a waveguide with fixed phase-shifting due to the inaccurate length and width. Therefore, a more practical approach is to use thermo-optic or electro-optic effects to make adjustable phase shifters. The advantage of the adjustable phase shifters is that the fabrication error of t can be adjusted by $\Delta\phi$. Hence in actual fabrication, the power of FH depends on t. The effective interval for t^2 is (0.6, 1). In this interval the suppression of SHD and IMD3 will not be affected, but only the power of FH will be affected. This is a relatively sufficient tolerance; simple process design is required to ensure that t^2 is in this interval. We can set an adjustable t^2 to maximize the power of FH. However, because t^2 and $\Delta\phi$ affect each other, if both parameters are adjustable, the device will be more unstable. When the environment or experimental conditions change, it is necessary to adjust the two parameters at the same time to make them match each other, which increases the difficulty of adjustment. For such comprehensive considerations, we recommend fixing t^2.

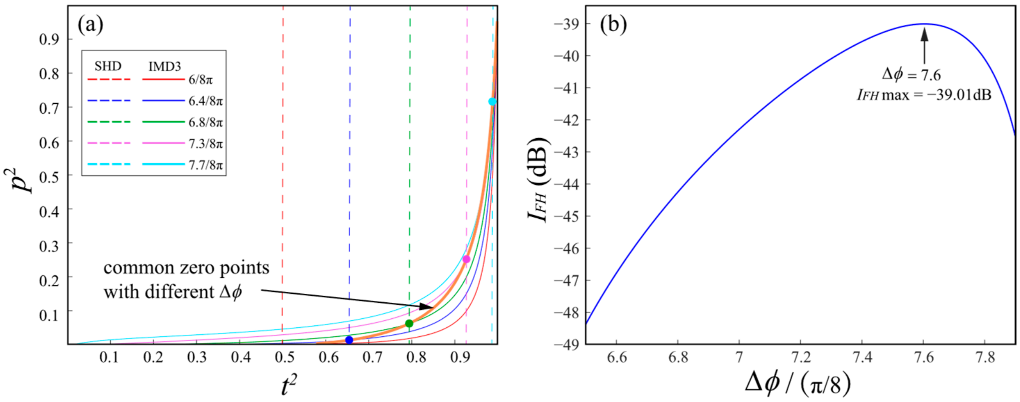

Figure 4. (**a**) The zero points of SHD and IMD3 with different $\Delta\phi$s. The orange line is the common zero points with different $\Delta\phi$. (**b**) The I_{FH} as a function of $\Delta\phi$.

3. Results and Discussion

3.1. Ideal CS-AMZM Simulation

In this section, the CS-AMZM was analyzed under ideal conditions. We used Lumerical INTERCONNECT to simulate the proposed CS-AMZM. Following this, CS-AMZM is compared with a standard MZM under the same conditions. The device parameters in the simulation are shown in Table 1, and the simulation settings are shown in Table 2. The test link of CS-AMZM is shown in Figure 5.

Table 1. Device parameters used to calculate the CS-AMZM.

Symbol	Quantity	Value
P_{LD}	Laser power	20 dBm
η	Detector responsivity	0.7 A/W
NF	Noise floor	−162 dBm/Hz
V_π	Half-wave voltage	4 V

Table 2. Simulation settings used to calculate the CS-AMZM.

Quantity	Value
Bitrate	2.5×10^{10} bit/s
Time window	2.56×10^{12} Hz
Sample rate	5.12×10^{10} s
Number of samples	131,072

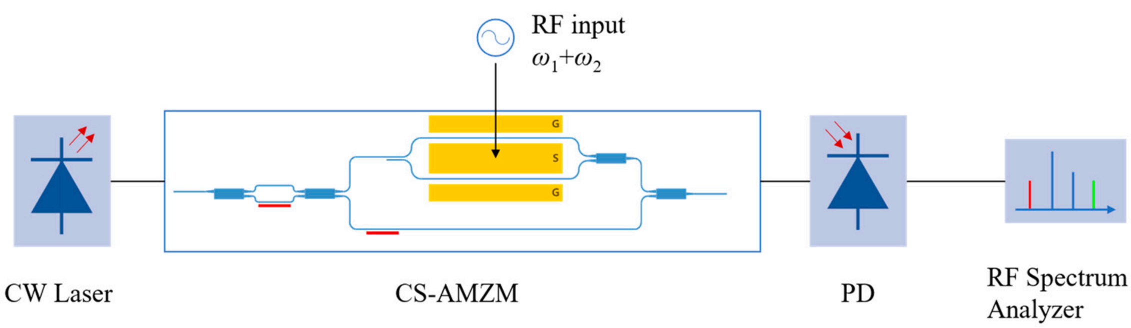

Figure 5. Simulation setup for CS-AMZM testing.

In the simulation, the solver settings are default, and losses are not considered, and the phase differences among WG-A1, WG-A2, and WG-CS are not considered. The linear operating point of the CS-AMZM is the same as calculated in the previous section. $\Delta\phi$ is set to $7.6/8\pi$, corresponding to achieving the common zero points of SHD and IMD3. The RF input power is 7 dBm. The frequency of the two-tone signal is set to 10 GHz and 11.25 GHz. We disabled the thermal noise of the laser and detector to detect the harmonics with eminently low power. This only eliminates white noise, which does not affect harmonic generation. Meanwhile, we adjusted the sensitivity of the RF spectrum analyzer to -200 dBm. When calculating SFDR, the NF is set to -162 dBm/Hz, which can be obtained in the experiment [15].

$$I_{TH,3} \sim \frac{1}{96} p \left(8ptk + \sqrt{2} q (k \cos \Delta\phi + t \sin \Delta\phi) \right) x_0^3, \tag{7}$$

The TH and IMD3 components have the same zero points. In the 5-octave range, the harmonics and intermodulation of the signal will be much lower than that of MZM and other linearized modulators, which do not consider SHD cancellation.

Simulated SFDR results of the standard MZM and the proposed CS-AMZM are shown in Figure 6c. Compared with MZM, although the FH power of the CS-AMZM is reduced, the $\text{SFDR}_{\text{IMD3}}$ is improved by 14 dB, and the SFDR_{SHD} is improved by 2.8 dB due to the complete suppression of harmonics. We note that the slopes of IMD3 power versus input power is ~5 for the CS-AMZM, because we have almost completely suppressed the third-order nonlinear components under small-signal conditions. Therefore, the main component of IMD3 is fifth-order nonlinear components. The fifth-order nonlinear component of IMD3 is calculated as (see Appendix B):

$$I_{IMD3,5} \sim -p^2 tk \left(2J_0 J_1 J_2^2 + 2J_0 J_1^2 J_3 + J_1^3 J_2 \right), \tag{8}$$

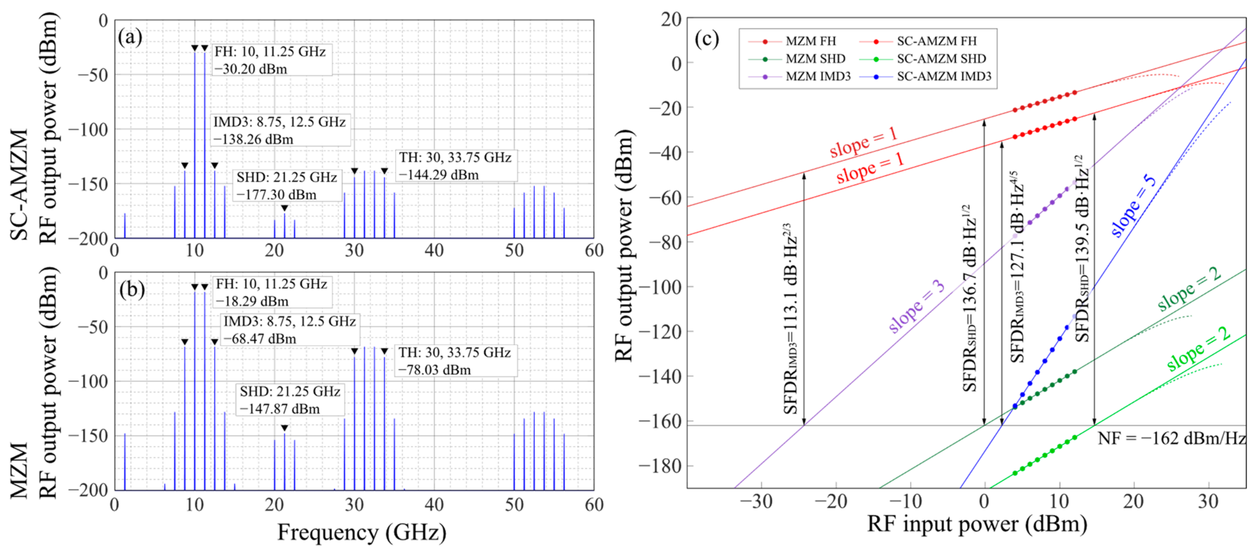

Figure 6. Spectrogram of (**a**) CS-AMZM and (**b**) MZM under ideal conditions. (**c**) Simulated SFDR results of the standard MZM and the proposed CS-AMZM. The dashed line shows the actual output power for large input power.

Fifth-order nonlinear components are not affected by separated carriers and have no zero points, which defines the linearization limit of CS-AMZM.

We performed a tolerance analysis of p^2 and $\Delta\phi$ with an RF input power of 10 dBm, as shown in Figure 7. The influence of p^2 offset on each component is given in Figure 7a, which shows that p^2 has little influence on FH and SHD. As mentioned in 3.2 in the manuscript, for large input signals, the minimum power of IMD3 is not at the optimal linear point, and the increase in IMD3 is less than 10dB when the offset of p^2 is between -0.004 and 0.008. Figure 7b shows the effect of the offset of $\Delta\phi$ on each component. It can be seen that a slight change in $\Delta\phi$ leads to a large increase in SHD. Therefore, in practical application, the accuracy and stability of $\Delta\phi$ should be ensured first, to obtain higher $SFDR_{SHD}$. If only IMD3 needs to be suppressed, the accuracy requirements for both p^2 and $\Delta\phi$ are drastically reduced.

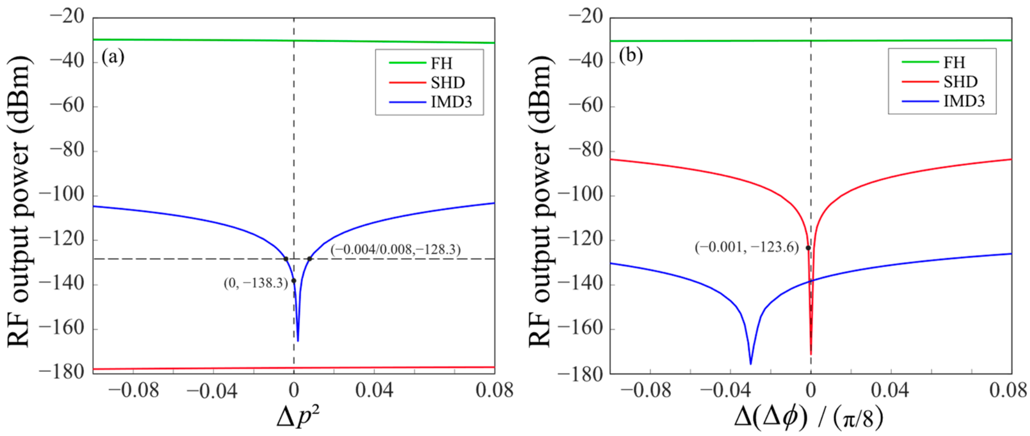

Figure 7. Tolerance of the CS-AMZM with the deviation of (**a**) p^2 and (**b**) $\Delta\phi$.

3.2. The Case of Large RF Input Power

As shown in the dashed line in Figure 6c, Bessel expansion does not satisfy linear approximation at large-signal conditions, and the beat higher-order nonlinear components cannot be neglected. In order to perform the calculation for the large-signal case, we abandon the approximation of the Bessel function and add the fifth-order beat frequency components in IMD3 (see Equation (8)). The normalized photocurrent under a small-signal condition (x_0 = 0.001) and large-signal condition (x_0 = 1) is shown in Figure 8. The zero points are shifted in the large-signal condition for both FH and IMD3 components. The zero points of the SHD are almost constant.

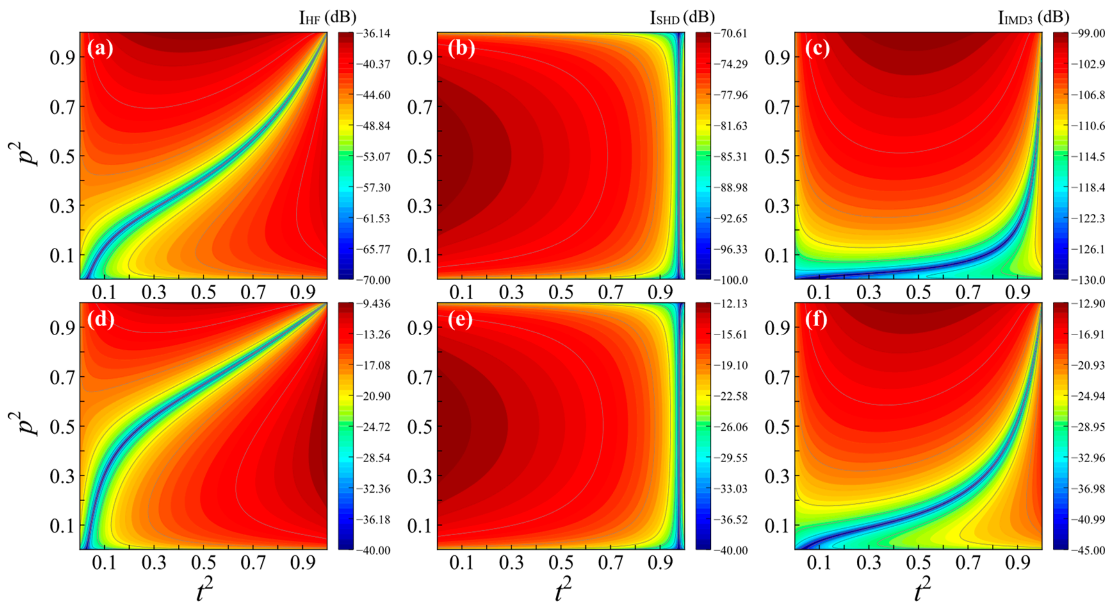

Figure 8. Contour map of the photocurrent as a function of t^2 and p^2 at (**a**–**c**) x_0 = 0.001 and (**d**–**f**) x_0 = 1.

The linearization condition is t^2 = 0.976 and p^2 = 0.550 when the input power is 13 dBm. The input power is scanned under this condition, and the result is shown in Figure 9. The input power corresponding to the position of the notch is exactly the input power. The slope is three for less than the input power and five for more. IMD3 contains all nonlinear components of an odd order. Higher-order nonlinear components have lower power. When the operating point slightly deviates from the condition of complete suppression of the third-order nonlinear components, the power of the third-order and fifth-order components are close. Therefore, the IMD3 for small input power is dominated by the third-order nonlinear components, while the IMD3 for large input power is dominated by the fifth-order nonlinear components. The intersection of the two extension lines is the position of the notch. In this case, the third- and fifth-order nonlinear components are almost equal. It can be seen from Equations (6) and (8) that the third- and fifth-order components are inverted. They are almost entirely canceled out when the power is equal, forming the notch.

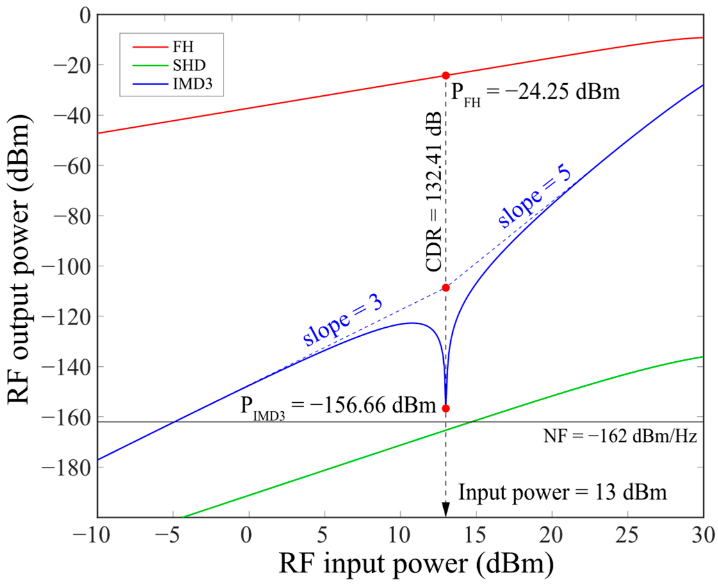

Figure 9. Output FH, SHD, and IMD3 powers versus input RF powers.

This phenomenon means that intermodulation distortions can be further suppressed at large signals by improving the feedback-control system. If a fixed control point is used, a high SFDR can be obtained. If adaptive control of the smallest harmonics can be achieved, an operating point with the minimum IMD3 power can be found by adjusting p^2 under large signals. Consequently, the modulator's carrier-to-distortion ratio (CDR) under large signals can be significantly improved.

3.3. Influence of Losses and Fabrication Deviations

The losses and deviations in fabrication are considered in this section. At the same time, the process of determining linear operating points is also simulated. There are many variable parameters in CS-AMZM, so we use a set of deviated parameters as an example to demonstrate the fabrication tolerance of CS-AMZM.

Common thin-film lithium niobate (TFLN) ridge waveguides are used to constitute the CS-AMZM. TFLN is 600 nm thick, the width of the ridge waveguide is 1 μm, the height is 300 nm, and the side wall inclination is 70°. We use the Lumerical FDE solver to simulate the waveguide. The effective refractive index of the waveguide is 1.907, and the group index is 2.266. We refer to the parameters in [26]; the voltage-length product is 2.2 V·cm, the loss of the WG is 0.3 dB/cm, and the loss of DCS is 0.5 dB. t^2 is set to 0.95 to simulate DCS fabrication deviation. The lengths of WG-A1, WG-A2, and WG-CS are 8800 μm, 8820 μm, and 9000 μm, respectively. The waveguide length is set in this way to simulate the fabrication error of the waveguide. According to Section 3.2, the large signal will offset the operating point, so we used an input signal of −10 dBm to find the linear operating point. The process is shown in Figure 10.

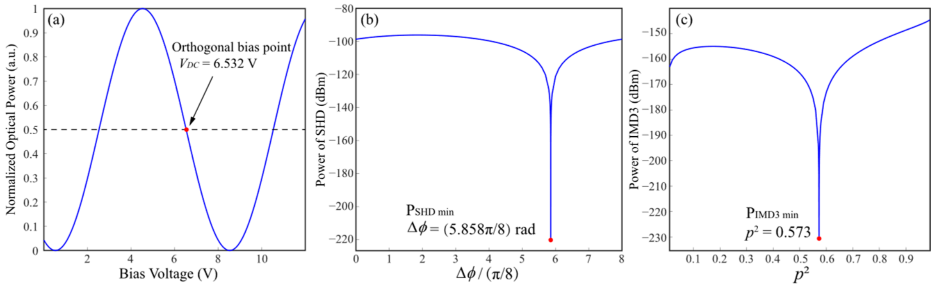

Figure 10. The process of finding the linear operating point: (**a**) V_{DC}, (**b**) $\Delta\phi$, and (**c**) p^2.

However, if only the E_{out} is monitored, the p^2 and $\Delta\phi$ cannot be determined. Therefore, a detector is needed to find the optimal working point. Firstly, the orthogonal bias point of AMZM can be found by the normalized output optical power, and the corresponding bias voltage can be obtained. Following this, since the suppression of SHD is independent of p^2, $\Delta\phi$ can be adjusted independently to find the operating point of SHD suppression. Finally, p^2 is adjusted to suppress IMD3. It should be noted that the adjustable beam splitter uses two 2 × 2 MMIs, thus ensuring that the initial phase difference of the two output ports is always π when adjusting p^2. Therefore, the adjustment of $\Delta\phi$ in step b will not be affected by adjusting p^2.

At the linear operating point, the spectrogram and SFDR results are shown in Figure 11. After introducing losses and deviations, the power of all frequency components is reduced by ~7 dB, caused by the waveguide loss. The dynamic range is reduced accordingly. Besides the losses, CS-AMZM performs the same as the ideal case. Therefore, we demonstrated that CS-AMZM can still suppress SHD and IMD3 well under non-ideal conditions.

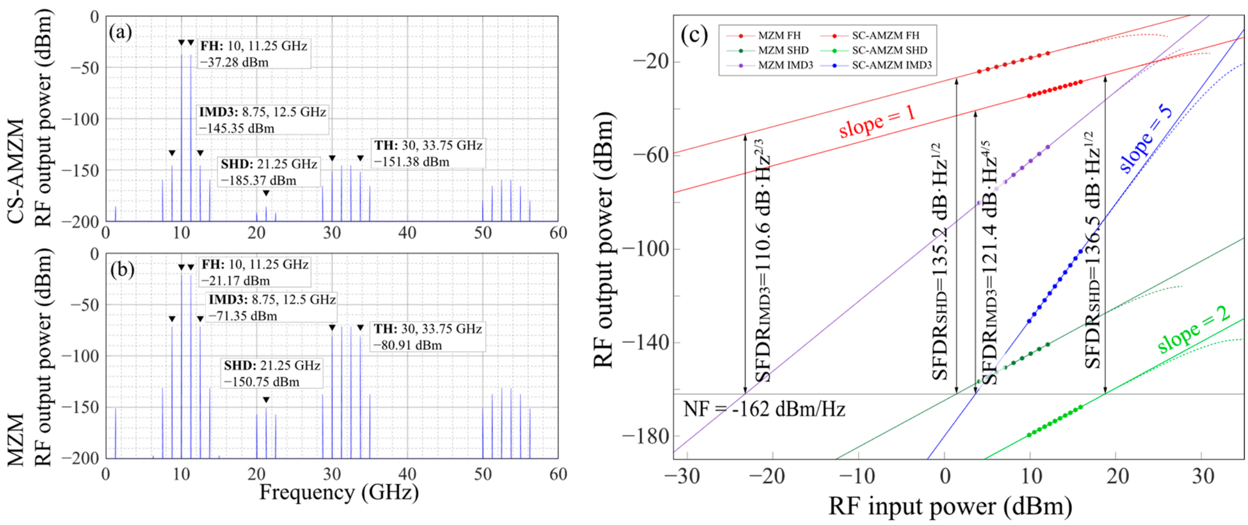

Figure 11. Spectrogram of (**a**) CS-AMZM and (**b**) MZM with losses and deviations. (**c**) Simulated SFDR results of the standard MZM and the proposed CS-AMZM. The dashed line shows the actual output power for large input power.

4. Conclusions

In summary, we proposed a novel, all-optical linearized modulator model suitable for the integration platform. A comparison of reported SFDRs for TFLN modulators is shown in Table 3; compared to those reported MZMs on LNOI platforms, the proposed CS-AMZM takes advantage of its simplicity and high performance.

Table 3. Comparison of the reported modulators on TFLN platforms.

Platform	Types	Parameters that Need to Be Controlled	SFDR dB·Hz$^{2/3}$	Ref.
Si/TFLN	MZM	1	99.6	[27]
Si/TFLN	MRM [1]	1	98.1	[19]
etched TFLN	Dual-Parallel-MZM	5	110.7	[10]
etched TFLN	Ring-assisted-MZM	3	120.04	[15]
etched TFLN	GAMIM [2]	2	101.2	[28]
etched TFLN (simulation)	CS-AMZM	3	121.4	This work

[1] MRM: Micro-ring modulator. [2] GAMIM: Grating-assisted Michelson interferometer modulator.

The scheme takes advantage of integrated device design flexibility, designing a CS-AMZM to suppress SHD and IMD3 components simultaneously, and even the TH component is suppressed. The novel structure leads to an $SFDR_{IMD3}$ improvement of ~14 dB and an $SFDR_{SHD}$ improvement of ~3 dB compared with a standard MZM. The dynamic range is improved throughout the whole operating bandwidth. For the case of large RF input power, CDR can be further increased by adjusting the power ratio of the splitter. We also demonstrated that CS-AMZM can still suppress SHD and IMD3 well under non-ideal conditions. Even though the only weakness is that CS-AMZM requires precise control of the operating point to achieve the best linearization, which requires high precision feedback control circuits, the all-optical structure and traditional ground-signal-ground (GSG) electrode simplify the application. The proposed CS-AMZM has the potential to directly replace MZM in analog signal system and achieve high-linearity modulation. It can be used in large-scale functional microwave photonic integrated circuits, microwave photonic radar, and other applications, leading to huge potential as a building block in the integrated microwave photonics system.

Author Contributions: Conceptualization, Y.Z. and J.L. (Jinye Li); methodology, software, writing—original draft preparation, Y.Z.; writing—review and editing, Z.X. and J.L. (Jianguo Liu); supervision, project administration, J.L. (Jianguo Liu). All authors have read and agreed to the published version of the manuscript.

Funding: This work is supported by the National Natural Science Foundation of China (61727815).

Informed Consent Statement: Not applicable.

Data Availability Statement: No new data were created or analyzed in this study. Data sharing is not applicable to this article.

Acknowledgments: The authors are grateful to the State Key Laboratory on Integrated Optoelectronics, Institute of Semiconductors, Chinese Academy of Sciences and College of Materials Science and Opto-Electronic Technology, University of Chinese Academy of Sciences.

Conflicts of Interest: The funders had no role in the design of the study; in the collection, analyses, or interpretation of data; in the writing of the manuscript, or in the decision to publish the results.

Appendix A. Derivation of the Photocurrent of the FH, SHD, and IMD3 Components

In this section, we show the complete mathematical derivation process. To ensure the completeness of the narrative, some equations are repeated with the main text, which are renumbered here.

The input optical field of the AMZM is set as $E_{in} = E_0\exp(j\omega t)$, and the driving signals of the two arms consist of a two-tone signal and a DC bias, written as:

$$\begin{aligned} V_1 &= V_{DC} + v_0(\cos\omega_1 t + \cos\omega_2 t) \\ V_2 &= -v_0(\cos\omega_1 t + \cos\omega_2 t) \end{aligned} \tag{A1}$$

where v_0 is the amplitude of the RF signal, V_{DC} is the voltage of the DC bias, and ω_1 and ω_2 are the angular frequencies of the two-tone signal. Here, to simplify the calculation, we let DC voltage only exist in the upper arm, which does not affect the correctness of the calculation.

Therefore, the modulated optical field of the two arms can be written as:

$$\begin{aligned} E_1 &= E_0 t \exp(j(\omega t + x_{DC} + x_0(\cos\omega_1 t + \cos\omega_2 t))) \\ E_2 &= E_0 k \exp(j(\omega t - x_0(\cos\omega_1 t + \cos\omega_2 t))) \end{aligned} \tag{A2}$$

where $x_0 = \pi v_0 / V_\pi$ and $x_{DC} = \pi V_{DC} / V_\pi$ are the modulator index of the RF signal and DC bias, respectively. V_π is the half-wave voltage of the AMZM. Bessel expansion of the Equation (A2) is calculated as [29]:

$$\begin{aligned} E_1 &= E_0 t \exp(j\omega t)\exp(jx_{DC}) \sum_{n=-\infty}^{\infty} J_n(x_0) j^n \exp(jn\omega_1 t) \sum_{n=-\infty}^{\infty} J_n(x_0) j^n \exp(jn\omega_2 t) \\ E_2 &= E_0 k \exp(j\omega t) \sum_{n=-\infty}^{\infty} J_n(x_0)(-j)^n \exp(jn\omega_1 t) \sum_{n=-\infty}^{\infty} J_n(x_0)(-j)^n \exp(jn\omega_2 t) \end{aligned} \tag{A3}$$

where J_n is the n-order Bessel function of the first kind. It can be seen that there are a series of frequency combinations of ω_1 and ω_2. We normalize E_0 to 1 and set the work point of AMZM to $\exp(jx_{DC}) = j$. Only the sidebands related to the FH, SHD, and IMD3 during modulating and detecting are considered, and the higher-order terms are ignored. Following this, the coefficients of the desired frequency components are extracted from the Equation (A3).

$$\begin{aligned} &[0]:\ W_0 = \tfrac{1}{2}(jt+k)J_0^2 \\ &[\pm\omega_1, \pm\omega_2]:\ W_1 = -\tfrac{1}{2}(t+jk)J_0 J_1 \\ &[\pm 2\omega_1, \pm 2\omega_2]:\ W_2 = -\tfrac{1}{2}(jt+k)J_0 J_2 \\ &[\pm(\omega_1-\omega_2)]:\ W_{11} = -\tfrac{1}{2}(jt+k)J_1^2 \\ &[\pm(2\omega_1-\omega_2), \pm(2\omega_2-\omega_1)]:\ W_{21} = \tfrac{1}{2}(t+jk)J_1 J_2 \end{aligned} \tag{A4}$$

where $[\omega_i]$ represents $\exp(j\omega t + j\omega_i t)$, and W_i is the power of the corresponding sideband. The photocurrent of a square-law detector can be expressed as:

$$\begin{aligned} I_{PD} &\sim E_{out} E_{out}^* \\ &= \begin{pmatrix} W_0[0] \\ +W_1[\pm\omega_1, \pm\omega_2] \\ +W_2[\pm 2\omega_1, \pm 2\omega_2] \\ +W_{11}[\pm(\omega_1-\omega_2)] \\ +W_{21}[\pm(2\omega_1-\omega_2), \pm(2\omega_2-\omega_1)] \end{pmatrix} \begin{pmatrix} W_0^*[0] \\ +W_1^*[\pm\omega_1, \pm\omega_2] \\ +W_2^*[\pm 2\omega_1, \pm 2\omega_2] \\ +W_{11}^*[\pm(\omega_1-\omega_2)] \\ +W_{21}^*[\pm(2\omega_1-\omega_2), \pm(2\omega_2-\omega_1)] \end{pmatrix} \end{aligned} \tag{A5}$$

The relationship between photocurrent and modulation sideband is shown in Figure A1.

Referencing Figure A1 and expanding Equation (A5), the photocurrent of the FH, SHD, and IMD3 can be written as:

$$\begin{aligned} I_{FH} &\sim |W_0 W_1^* + W_1 W_0^*| \\ &= tkJ_0^3 J_1 \\ I_{SHD} &\sim |2(W_0 W_2^* + W_2 W_0^*) + W_1 W_1^* + W_1 W_1^*| \\ &= (t^2+k^2)\left(\tfrac{1}{2}J_0^2 J_1^2 - J_0^3 J_2\right) \\ I_{IMD3} &\sim |W_0 W_{21}^* + W_{21} W_0^* + W_1 W_{11}^* + W_{11} W_1^* + W_1 W_2^* + W_2 W_1^*| \\ &= tk\left(J_0^2 J_1 J_2 + \tfrac{1}{2}J_0 J_1^3\right) \end{aligned} \tag{A6}$$

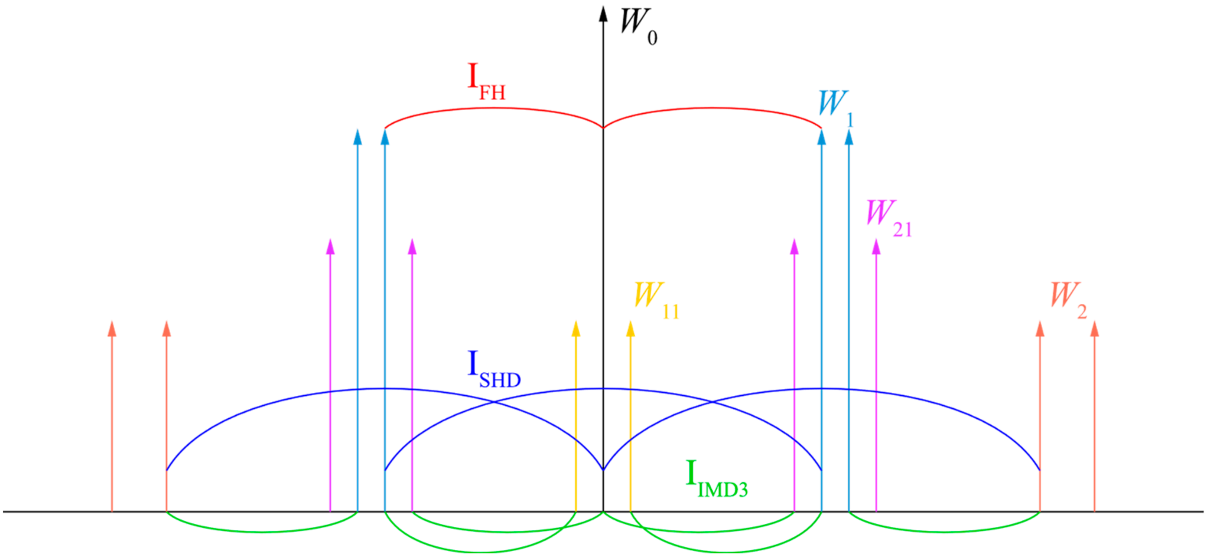

Figure A1. A schematic diagram of modulation sideband and photocurrent.

For the small signal ($x_0 \to 0$), the Bessel function is approximated by a power series expansion:

$$J_n(x) = \frac{1}{\Gamma(n+1)}\left(\frac{x}{2}\right)^n + O\left(x^{n+2}\right), x \to 0 \tag{A7}$$

which means $J_0 \approx 1$, $J_1 \approx x_0/2$, $J_2 \approx x_0^2/8$, and $J_3 \approx x_0^3/48$. Following this, Equation (A6) can be written as

$$\begin{aligned} I_{FH} &\sim \tfrac{1}{2}tkx_0 \\ I_{SHD} &\approx 0 \\ I_{IMD3} &\sim \tfrac{1}{8}tkx_0^3 \end{aligned} \tag{A8}$$

The derivation of CS-AMZM is similar with AMZM. An adjustable 1×2 splitter [30] was used to form the CS-AMZM. Two 2×2 MMI are used to form a 1×2 MZI to achieve the adjustable 1×2 splitter. The output power depends on the phase difference between the two arms:

$$\begin{aligned} \begin{bmatrix} E_{out1} \\ E_{out2} \end{bmatrix} &= \begin{bmatrix} \frac{\sqrt{2}}{2} & j\frac{\sqrt{2}}{2} \\ j\frac{\sqrt{2}}{2} & \frac{\sqrt{2}}{2} \end{bmatrix} \begin{bmatrix} \exp(j\Delta\varphi) & 0 \\ 0 & 1 \end{bmatrix} \begin{bmatrix} \frac{\sqrt{2}}{2} & j\frac{\sqrt{2}}{2} \\ j\frac{\sqrt{2}}{2} & \frac{\sqrt{2}}{2} \end{bmatrix} \begin{bmatrix} E_{in} \\ 0 \end{bmatrix} \\ &= \begin{bmatrix} \exp(j\Delta\varphi) - 1 \\ j(\exp(j\Delta\varphi) + 1) \end{bmatrix} E_{in} \end{aligned} \tag{A9}$$

where $\Delta\varphi$ is the phase difference between the two arms, Ein is the input electric field, and $E_{out1,2}$ are the output electric field of two output ports. The output power can be written as:

$$\begin{bmatrix} P_{out1} \\ P_{out2} \end{bmatrix} = \begin{bmatrix} |E_{out1}|^2 \\ |E_{out2}|^2 \end{bmatrix} = \begin{bmatrix} 1 - \cos(\Delta\varphi) \\ 1 + \cos(\Delta\varphi) \end{bmatrix} E_{in} \tag{A10}$$

Therefore, the output power can be adjusted by controlling the $\Delta\varphi$. The modulated optical field of the two arms and the separated carrier can be written as:

$$\begin{aligned} E_1 &= pt\exp(jx_{DC})\exp(j\omega t + jx_0(\cos\omega_1 t + \cos\omega_2 t)) \\ E_2 &= pk\exp(j\omega t - jx_0(\cos\omega_1 t + \cos\omega_2 t)) \\ E_3 &= q\Delta\phi \end{aligned} \tag{A11}$$

Bessel expansion of the Equation (A11) is calculated as:

$$\begin{aligned} E_1 &= E_0 pt \exp(j\omega t)\exp(jx_{DC}) \sum_{n=-\infty}^{\infty} J_n(x_0) j^n \exp(jn\omega_1 t) \sum_{n=-\infty}^{\infty} J_n(x_0) j^n \exp(jn\omega_2 t) \\ E_2 &= E_0 pk \exp(j\omega t) \sum_{n=-\infty}^{\infty} J_n(x_0)(-j)^n \exp(jn\omega_1 t) \sum_{n=-\infty}^{\infty} J_n(x_0)(-j)^n \exp(jn\omega_2 t) \end{aligned} \tag{A12}$$

Following this, the coefficients of the desired frequency components are extracted from the Equation (A12).

$$\begin{aligned} &W_0 = \tfrac{p}{2}(jt+k)J_0^2 + \tfrac{\sqrt{2}q}{2}\exp(j\Delta\phi) \to [0] \\ &W_1 = -\tfrac{p}{2}(t+jk)J_0 J_1 \to [\pm\omega_1, \pm\omega_2] \\ &W_2 = -\tfrac{p}{2}(jt+k)J_0 J_2 \to [\pm 2\omega_1, \pm 2\omega_2] \\ &W_{11} = -\tfrac{p}{2}(jt+k)J_1^2 \to [\pm(\omega_1-\omega_2)] \\ &W_3 = \tfrac{p}{2}(t+jk)J_1 J_2 \to [\pm(2\omega_1-\omega_2), \pm(2\omega_2-\omega_1)] \end{aligned} \tag{A13}$$

The photocurrent of the FH, SHD, and IMD3 of CS-AMZM can be written as:

$$\begin{aligned} I_{FH} \quad &\sim \left| p^2 kt J_0^2 + \tfrac{\sqrt{2}}{2} pq(t\cos\Delta\phi + k\sin\Delta\phi) \right| J_0 J_1 \\ &= \tfrac{1}{2} p \left| 2pkt + \sqrt{2}q(t\cos\Delta\phi + k\sin\Delta\phi) \right| x_0 \\ I_{SHD} \quad &\sim \left| (p^2t^2 + p^2k^2)\left(\tfrac{1}{2}J_0^2 J_1^2 - J_0^3 J_2\right) - \sqrt{2} J_0 J_2 pq(k\cos\Delta\phi + t\sin\Delta\phi) \right| \\ &= \tfrac{\sqrt{2}}{4} pq |k\cos\Delta\phi + t\sin\Delta\phi| x_0^2 \\ I_{IMD3} \quad &\sim \left| p^2 tk\left(J_0^2 J_1 J_2 + \tfrac{1}{2} J_0 J_1^3\right) + \tfrac{\sqrt{2}}{4} J_1 J_2 pq(k\cos\Delta\phi + t\sin\Delta\phi) \right| \\ &= \tfrac{1}{64} p \left| 8ptk + \sqrt{2}q(k\cos\Delta\phi + t\sin\Delta\phi) \right| x_0^3 \end{aligned} \tag{A14}$$

As shown in Figure 6, the FH of CS-AMZM is reduced compared with the standard MZM. There are two reasons for the decrease in FH. Firstly, compared with the standard MZM, the FH of AMZM will be reduced, which is due to the reduction in the extinction ratio caused by the asymmetric interference. Secondly, after the introduction of the adjustable 1×2 beam splitter, compared with the IFH in Equations (A8) and (A14), less light is involved in the modulation due to the separation of part of the carrier, which results in a reduction in FH.

Appendix B. Derivation of Higher-Order Sidebands and Nonlinear Component

In the main text, we mentioned the computations of large signals and TH, which needs to consider the higher-order sidebands. The power of associated sidebands can be written as:

$$\begin{aligned} &[\pm 3\omega_1, \pm 3\omega_2]: \ W_3 = \tfrac{p}{2}(t+jk)J_0 J_3 \\ &[\pm 4\omega_1, \pm 4\omega_2]: \ W_4 = \tfrac{p}{2}(jt+k)J_0 J_4 \\ &[\pm(3\omega_1+\omega_2), \pm(3\omega_1-\omega_2), \pm(3\omega_1-\omega_2)]: \ W_{31} = \tfrac{p}{2}(jt+k)J_1 J_3 \\ &[\pm 2(\omega_1+\omega_2), \pm 2(\omega_1-\omega_2)]: \ W_{22} = \tfrac{p}{2}(jt+k)J_2^2 \end{aligned} \tag{A15}$$

The third-order nonlinear component of TH is:

$$\begin{aligned} I_{TH,3} \quad &\sim W_0 W_3^* + W_3 W_0^* + W_1 W_2^* + W_2 W_1^* \\ &= p^2 tk(2J_0^3 J_3 + J_0^2 J_1 J_2) + \tfrac{\sqrt{2}}{2} J_3 pq(k\cos\Delta\phi + t\sin\Delta\phi) \\ &= \tfrac{1}{96} p\left(8ptk + \sqrt{2}q(k\cos\Delta\phi + t\sin\Delta\phi)\right) x_0^3 \end{aligned} \tag{A16}$$

The fifth-order nonlinear component of IMD3 is:

$$\begin{aligned} I_{IMD3,5} &\sim W_2W_{21}^* + W_{21}W_2^* + W_{21}W_{11}^* + W_{11}W_{21}^* + W_1W_{22}^* + W_{22}W_1^* + W_3W_{11}^* + W_{11}W_3^* \\ &+W_1W_{31}^* + W_{31}W_1^* \\ &= -p^2tk\left(2J_0J_1J_2^2 + 2J_0J_1^2J_3 + J_1^3J_2\right) \end{aligned} \tag{A17}$$

References

1. Li, M.; Zhu, N. Recent Advances in Microwave Photonics. *Front. Optoelectron.* **2016**, *9*, 160–185. [CrossRef]
2. Marpaung, D.; Yao, J.; Capmany, J. Integrated Microwave Photonics. *Nat. Photonics* **2019**, *13*, 80–90. [CrossRef]
3. Capmany, J.; Munoz, P. Integrated Microwave Photonics for Radio Access Networks. *J. Light. Technol.* **2014**, *32*, 2849–2861. [CrossRef]
4. Cox, C.H.; Ackerman, E.I.; Betts, G.E.; Prince, J.L. Limits on the Performance of RF-over-Fiber Links and Their Impact on Device Design. *IEEE Trans. Microw. Theory Techn.* **2006**, *54*, 906–920. [CrossRef]
5. Chou, H.F.; Ramaswamy, A.; Zibar, D.; Johansson, L.A.; Bowers, J.E.; Rodwell, M.; Coldren, L.A. Highly Linear Coherent Receiver with Feedback. *IEEE Photon. Technol. Lett.* **2007**, *19*, 940–942. [CrossRef]
6. Sadhwani, R.; Jalali, B. Adaptive CMOS Predistortion Linearizer for Fiber-Optic Links. *J. Light. Technol.* **2003**, *21*, 3180–3193. [CrossRef]
7. Zhang, G.; Zheng, X.; Li, S.; Zhang, H.; Zhou, B. Postcompensation for Nonlinearity of Mach–Zehnder Modulator in Radio-over-Fiber System Based on Second-Order Optical Sideband Processing. *Opt. Lett.* **2012**, *37*, 806. [CrossRef]
8. Zhang, G.; Li, S.; Zheng, X.; Zhang, H.; Zhou, B.; Xiang, P. Dynamic Range Improvement Strategy for Mach-Zehnder Modulators in Microwave/Millimeter-Wave ROF Links. *Opt. Express* **2012**, *20*, 17214. [CrossRef]
9. Khilo, A.; Sorace, C.M.; Kärtner, F.X. Broadband Linearized Silicon Modulator. *Opt. Express* **2011**, *19*, 4485. [CrossRef]
10. Huang, X.; Liu, Y.; Tu, D.; Yu, Z.; Wei, Q.; Li, Z. Linearity-Enhanced Dual-Parallel Mach–Zehnder Modulators Based on a Thin-Film Lithium Niobate Platform. *Photonics* **2014**, *9*, 197. [CrossRef]
11. Zhou, Y.; Zhou, L.; Wang, M.; Xia, Y.; Zhong, Y.; Li, X.; Chen, J. Linearity Characterization of a Dual–Parallel Silicon Mach–Zehnder Modulator. *IEEE Photonics J.* **2016**, *8*, 7805108. [CrossRef]
12. Zhang, Q.; Yu, H.; Jin, H.; Qi, T.; Li, Y.; Yang, J.; Jiang, X. Linearity Comparison of Silicon Carrier-Depletion-Based Single, Dual-Parallel, and Dual-Series Mach–Zehnder Modulators. *J. Light. Technol.* **2018**, *36*, 3318–3331. [CrossRef]
13. Zhang, Q.; Yu, H.; Xia, P.; Fu, Z.; Wang, X.; Yang, J. High Linearity Silicon Modulator Capable of Actively Compensating Input Distortion. *Opt. Lett.* **2020**, *45*, 3785. [CrossRef]
14. Morton, P.A.; Khurgin, J.B.; Morton, M.J. All-Optical Linearized Mach-Zehnder Modulator. *Opt. Express* **2021**, *29*, 37302. [CrossRef]
15. Feng, H.; Zhang, K.; Sun, W.; Ren, Y.; Zhang, Y.; Zhang, W.; Wang, C. Ultra-High-Linearity Integrated Lithium Niobate Electro-Optic Modulators. *Photonics Res.* **2022**, *10*, 2366. [CrossRef]
16. Yang, J.; Wang, F.; Jiang, X.; Qu, H.; Wang, M.; Wang, Y. Influence of Loss on Linearity of Microring-Assisted Mach-Zehnder Modulator. *Opt. Express* **2004**, *12*, 4178. [CrossRef]
17. Tazawa, H.; Steier, W.H. Bandwidth of Linearized Ring Resonator Assisted Mach-Zehnder Modulator. *IEEE Photonics Technol. Lett.* **2005**, *17*, 1851–1853. [CrossRef]
18. Ayazi, A.; Baehr-Jones, T.; Liu, Y.; Lim, A.E.J.; Hochberg, M. Linearity of Silicon Ring Modulators for Analog Optical Links. *Opt. Express* **2012**, *20*, 13115. [CrossRef]
19. Chen, L.; Chen, J.; Nagy, J.; Reano, R.M. Highly Linear Ring Modulator from Hybrid Silicon and Lithium Niobate. *Opt. Express* **2015**, *23*, 13255. [CrossRef]
20. Zhang, C.; Morton, P.A.; Khurgin, J.B.; Peters, J.D.; Bowers, J.E. Ultralinear Heterogeneously Integrated Ring-Assisted Mach–Zehnder Interferometer Modulator on Silicon. *Optica* **2016**, *3*, 1483. [CrossRef]
21. Chen, S.; Zhou, G.; Zhou, L.; Lu, L.; Chen, J. High-Linearity Fano Resonance Modulator Using a Microring-Assisted Mach–Zehnder Structure. *J. Light. Technol.* **2020**, *38*, 3395–3403. [CrossRef]
22. Khurgin, J.B.; Morton, P.A. Linearized Bragg Grating Assisted Electro-Optic Modulator. *Opt. Lett.* **2014**, *39*, 6946. [CrossRef] [PubMed]
23. Zhang, J.; Han, L.; Kuo, B.P.P.; Radic, S. Broadband Angled Arbitrary Ratio SOI MMI Couplers with Enhanced Fabrication Tolerance. *J. Light. Technol.* **2020**, *38*, 5748–5755. [CrossRef]
24. Deng, Q.; Liu, L.; Li, X.; Zhou, Z. Arbitrary-Ratio 1×2 Power Splitter Based on Asymmetric Multimode Interference. *Opt. Lett.* **2014**, *39*, 5590. [CrossRef] [PubMed]
25. Sharma, B.; Kishor, K.; Pal, A.; Sharma, S.; Makkar, R.; Pal, A.; Kumar, S.; Sharma, S.; Raghuwanshi, S.K. Design and Simulation of Ultra-Low Loss Triple Tapered Asymmetric Directional Coupler at 1330 Nm. *Microelectron. J.* **2021**, *107*, 104957. [CrossRef]
26. Wang, C.; Zhang, M.; Chen, X.; Bertrand, M.; Shams-Ansari, A.; Chandrasekhar, S.; Winzer, P.; Lončar, M. Integrated Lithium Niobate Electro-Optic Modulators Operating at CMOS-Compatible Voltages. *Nature* **2018**, *562*, 101–104. [CrossRef]
27. He, M.; Xu, M.; Ren, Y.; Jian, J.; Ruan, Z.; Xu, Y.; Gao, S.; Sun, S.; Wen, X.; Zhou, L.; et al. High-Performance Hybrid Silicon and Lithium Niobate Mach–Zehnder Modulators for 100 Gbit S−1 and Beyond. *Nat. Photonics* **2019**, *13*, 359–364. [CrossRef]

28. Ghoname, A.O.; Hassanien, A.E.; Chow, E.; Goddard, L.L.; Gong, S. Highly Linear Lithium Niobate Michelson Interferometer Modulators Assisted by Spiral Bragg Grating Reflectors. *Opt. Express* **2022**, *30*, 40666. [CrossRef]
29. Watson, G.N. *A Treatise on the Theory of Bessel Functions*, 2nd ed.; Cambridge Mathematical Library, Ed.; Cambridge University Press: Cambridge, UK; New York, NY, USA, 1995; ISBN 978-0-521-48391-9.
30. Pal, A.; Kumar, S.; Sharma, S.; Raghuwanshi, S.K. Design of 4 to 2 Line Encoder Using Lithium Niobate Based Mach Zehnder Interferometers for High Speed Communication. In Proceedings of the Optical Modelling and Design IV, Brussels, Belgium, 27 April 2016; Wyrowski, F., Sheridan, J.T., Meuret, Y., Eds.; p. 98890H.